UC Berkeley

Title

Novel Structural Motif To Promote Mg-Ion Mobility: Investigating ABO4 Zircons as Magnesium Intercalation Cathodes

Authors

Rutt, Ann
Sari, Dogancan
Chen, Qian
et al.

Copyright Information

Peer reviewed

Novel Structural Motif To Promote Mg-Ion Mobility: Investigating ABO$_4$ Zircons as Magnesium Intercalation Cathodes

Ann Rutt,[§] Dogancan Sari,[§] Qian Chen, Jiyoon Kim, Gerbrand Ceder, and Kristin A. Persson*

Cite This: ACS Appl. Mater. Interfaces 2023, 15, 34983−34991

Read Online

ACCESS | Metrics & More | Article Recommendations | Supporting Information

ABSTRACT: There is an increasing need for sustainable energy storage solutions as fossil fuels are replaced by renewable energy sources. Multivalent batteries, specifically Mg batteries, are one energy storage technology that researchers continue to develop with hopes to surpass the performance of Li-ion batteries. However, the limited energy density and transport properties of Mg cathodes remain critical challenges preventing the realization of high-performance multivalent batteries. In this work, ABO$_4$ zircon materials (A = Y, Eu and B = V, Cr) are computationally and experimentally evaluated as Mg intercalation cathodes. Remarkably good Mg-ion transport properties were predicted and Mg-ion intercalation was experimentally verified in sol−gel synthesized zircon YVO$_4$, EuVO$_4$, and EuCrO$_4$. Among them, EuVO$_4$ exhibited the best electrochemical performance and demonstrated repeated reversible cycling. While we believe that the one-dimensional diffusion channels and redox-active species tetragonal coordination limit the value of many zircons as high-performance cathodes, their unique structural motif of overlapping polyhedra along the diffusion pathway appears instrumental for promoting good Mg-ion mobility. The motif results in a favorable "6-5-4" change in coordination that avoids unfavorable sites with lower coordination along the diffusion pathway and a structural design metric for future Mg cathode development.

KEYWORDS: cathodes, magnesium batteries, energy storage, diffusion, multivalent ion mobility
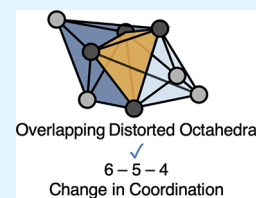
INTRODUCTION

Multivalent batteries are one of several emerging "beyond Li-ion" battery energy storage technologies that aim to enable large-scale renewable energy.[1−4] Of the multivalent battery chemistries (Mg^{2+}, Ca^{2+}, Zn^{2+}, Al^{3+}, etc.), the most progress has been made with magnesium batteries since the first lab-scale prototype magnesium cell was reported in 2000 using a Mg$_x$Mo$_6$S$_8$ Chevrel cathode.[1] Research efforts continue to focus on improving Mg cathodes in order to identify materials with suitable energy density and rate capability for high-performance batteries.[6−8] While progress has been made, the best available Mg cathodes exhibit inferior voltages as compared to state-of-the-art Li cathodes, and poor solid-state mobility, which results in insufficient rate capability.[2] The identification of high-performance Mg cathodes is an issue that must be overcome in order to realize a Mg battery chemistry that can outperform Li-ion batteries and warrant commercialization.[3−5]

Given the transport challenges inherent to more polarizing multivalent ions (compared to Li$^+$), recent efforts have been dedicated to understanding and improving the solid-state mobility of multivalent ions, especially in oxide hosts. Common material design strategies[5] include: (1) using materials with larger anions, which allow for better screening, in the host framework (e.g., opting for sulfides or selenides over oxides) and (2) leveraging the coordination preference of a specific cation to improve transport. For example, Mg^{2+} has a strong preference for octahedral local bonding environments,[6,7] which usually results in poor mobility and difficult extraction of Mg^{2+} from octahedral sites.

High energy sites along the diffusion pathway in a material can also correspond to the mobile cation passing through points of lower coordination. These lower coordination points may represent a position where the mobile cation passes through a plane of neighboring anions.[2] For example, in the structural motif where a diffusion pathway is composed of edge-sharing octahedra as illustrated in Figure 1a, the lowest coordination occurs when the mobile cation passes through a triangular plane of 3 anions. This triangular plane is the shared face between the octahedral and intermediate tetrahedral site and corresponds to the highest energy point along the migration pathway in several materials with this edge-sharing octahedral motif.[8] Materials with larger anions of the same charge are better at screening unfavorable electrostatic interactions at these bottlenecks which usually results in improved transport properties.[9−11] While understanding the connection between various material's properties and multivalent ion transport is evolving, identifying materials with better transport properties based on these principles remains a challenge.
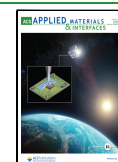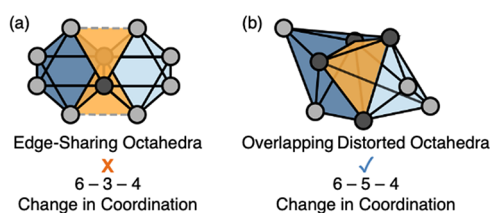
Figure 1. Visual representation of the characteristic structural motifs along diffusion pathways where the gray circles represent anions. Neighboring octahedral sites are colored with different shades of blue, while the intermediate tetrahedral sites are colored yellow. The darker gray-colored circles indicate which anions are shared by both octahedra. Panel (a) shows the edge-sharing octahedral motif found in previously studied cathodes (e.g., spinels, layered structures, and olivines) where there is no shared volume with the intermediate tetrahedral site. Panel (b) shows the overlapping distorted octahedral motif characteristic of zircons where volume is shared with the intermediate tetrahedral site.

Our work introducing a computational screening approach to identify high-performance multivalent intercalation cathodes[9] has proved instrumental in evaluating solid-state mobility in a wider variety of structure types. A new family of materials with the ABO_4 zircon-type structure (with tetragonal space group $I41/amd$) was identified using this methodology, specifically for their predicted high Mg^{2+} mobility. Our subsequent investigation of these materials as Mg cathodes is reported in this work. The ABO_4 zircon structure is composed of edge-sharing alternating AO_8 dodecahedrons and BO_4 tetrahedrons and is illustrated in Figure 2, a depiction of the unit cell structure of zircon YVO_4.
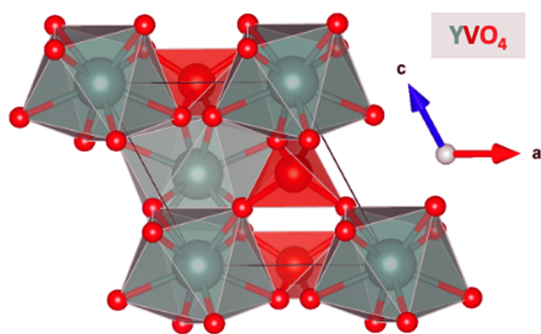

Figure 2. Unit cell structure of YVO_4 showing the ABO_4 zircon-type structure (with tetragonal space group $I41/amd$) composed of edge-sharing alternating AO_8 dodecahedrons and BO_4 tetrahedrons.

In the AO_8 dodecahedron, the A atom is 8-coordinated, while in the BO_4 tetrahedron, the B atom is 4-coordinated. These structures also exhibit interstitial sites of distorted octahedra and tetrahedrons, forming one-dimensional channels,[12] which are presented in Figure 1b.

As illustrated in Figure 1, zircons present a unique structural motif compared to many previously studied cathodes (e.g., spinels, layered structures, and olivines) with edge-sharing octahedral sites.[8] A key difference is that the tetrahedral and distorted octahedral interstitial sites of the zircon structure are overlapping in volume, in contrast to the absence of shared volume in materials with edge-sharing octahedral interstitial sites, connected by face-sharing tetrahedral sites. The prototype zircon is $ZrSiO_4$, a naturally occurring mineral,[13] although ABO_4 zircons span a wide range of chemistries. This

work focuses on a smaller subset of zircons (A = Y, Eu and B = V, Cr) which contain a redox-active cation and can be synthesized through previously reported methods.

The four zircon materials, which are the focus of this work, have been available in the Materials Project with standard properties calculated by density functional theory (DFT).[14] In addition, the structural, mechanical, electronic, magnetic, and optical properties of zircons have previously been investigated, including YVO_4,[15,16] $EuVO_4$,[17−19] $YCrO_4$,[13,20] and $EuCrO_4$.[21,22] Comparatively, there is less work regarding the electrochemical and transport properties of zircons required to inform their performance as intercalation cathodes. Oxygen diffusivity has been measured for zircon $EuVO4$[18] and the conductivity of interstitial H^+, Li^+, Na^+, Mg^{2+}, and Ca^{2+}, was studied in zircon YPO_4[23,24] (although YPO_4 lacks a redox active species which is one of the requirements for a cathode). To our knowledge, this is the first reported work to consider zircon materials as intercalation cathodes for Mg.

■ RESULTS

Predicted Phase Stability upon Mg Intercalation. A previously developed computational method and associated workflow to predict insertion sites (here denoted the "insertion algorithm")[25] for host materials was used to evaluate the maximum viable concentration of Mg that could be introduced in zircon YVO_4, $EuVO_4$, $YCrO_4$, and $EuCrO_4$. This workflow performs successive DFT calculations of Mg-ion insertions at candidate interstitial sites, which are identified by charge density minima in the host structure determined by DFT calculations. The insertions are deemed successful as long as the relaxed discharged structure is similar (topotactic insertion) to the host structure as identified with the structure matcher module in pymatgen[26] and does not exceed the redox capability based on the contained transition metal. Given these criteria, this capacity should be taken as an upper bound for the real capacity that can be achieved.

The "energy above hull" measures the driving force for a phase to decompose into potentially more stable phases. For a given material, it is measured as the energy per atom above the convex energy hull defined by the most stable phases in the relevant chemical space.[27,28] The minimum value of this quantity, 0 eV/atom, indicates that a material is predicted to be the most thermodynamically stable phase at 0 K based on DFT calculations. Energy above hull values were calculated with the MP2020 compatibility scheme[29] and the Materials Project[14] database phase diagrams using pymatgen.[26] The energy above hull values for the Mg_xABO_4 zircons of interest (A = Y, Eu and B = V, Cr) are reported for 3 magnesium concentrations ($x = 0, 0.5, 1$) in Table 1. In addition, if a material is not in the most stable phase, the predicted decomposition products are included. Conversion voltages for the four zircons of interest were also calculated using pymatgen[26] and phase diagrams from the Materials Project.[14] The conversion voltages and their corresponding reactions are shown in Table 2.

The insertion algorithm identified a single Mg-ion insertion per unit cell (2 formula units) in $EuVO_4$ and $YCrO_4$, resulting in a maximum intercalation level of $Mg_{0.5}ABO_4$. A maximum intercalation level of $MgABO_4$ without any significant change in structure could be tolerated for YVO_4 and $EuCrO_4$, despite the high energy above the hull. The $ABO_4 \Leftrightarrow MgABO_4$ reaction is found to be more energetically favorable than $ABO_4 \Leftrightarrow Mg_{0.5}ABO_4$ which makes observing $Mg_{0.5}ABO_4$ unlikely. With the exception of $EuVO_4$, all energy above hull

Table 1. Energy Above Hull Values from DFT Calculations Combined with Materials Project[14] Data to Evaluate Phase Stability for Mg_xABO_4 Zircons (A = Y, Eu and B = V, Cr) at x = 0, 0.5, 1 Magnesium Concentrations[a]

ABO₄ Zircon	Phase Stability (meV/atom)			Decomposition Products
	ABO_4	$Mg_{0.5}ABO_4$	$MgABO_4$	
YVO₄ (mp-19133)	0	133	196	YVO₃ (mp-18883)
				MgO (mp-1265)
EuVO₄ (mp-22796)	0	0		
YCrO₄ (mp-18825)	~0[b]	139		Y₂O₃ (mp-2652)
				YCrO₄ (mp-18825)
				MgCr₂O₄ (mp-19202)
				MgCrO₄ (mp-19120)
EuCrO₄ (mp-22586)	0.1	127	219	Eu₂O₃ (mp-1182469)
				EuCrO₄ (mp-22586)
				MgCr₂O₄ (mp-19202)
				MgO (mp-1265)

[a]The decomposition products are included when a material was not in the most stable phase at that composition. [b]Within our numerical accuracy, YCrO₄ is degenerate with the hull.

Table 2. Conversion Reactions and Voltages Calculated from DFT for ABO_4 Zircons (A = Y, Eu and B = V, Cr)

Conversion Reaction	Conversion Voltage (V)
$2YVO_4 + 2Mg \rightarrow 2YVO_3 + 2MgO$	1.7
$2EuVO_4 + Mg \rightarrow Eu_2MgV_2O_8$	1.9
$2YcrO_4 + 1.25Mg \rightarrow Y_2O_3 + 0.5MgCrO_4 + 0.75MgCr_2O_4$	2.8
$2EuCrO_4 + 2Mg \rightarrow MgCr_2O_4 + Eu_2O_3 + MgO$	2.6

values upon magnesiation are >100 meV/atom, which strongly indicates that further magnesiation is unfavorable and will result in phase decomposition.[30,31] The best phase stability was found in EuVO₄, where both EuVO₄ and Mg₀.₅EuVO₄ were found to be the ground states with an energy above the hull of 0 meV/atom. The conversion voltages of YCrO₄ (2.8 V) and EuCrO₄ (2.6 V) are also significantly higher than those of YVO₄ (1.7 V) and EuVO₄ (1.9 V). Therefore, of the four zircons evaluated with DFT, Mg-ion intercalation is predicted to be most favorable in EuVO₄.

DFT-Predicted Battery Electrode Properties. The Python package, pymatgen,[26] was used to analyze the Mg electrode properties that can be determined from the DFT calculations generated by the insertion algorithm. These properties are reported in Table 3, which include voltage (compared to the Mg/Mg^{2+} redox couple), gravimetric capacity (based on the ABO₄ molar mass for the charged

composition without Mg), and the percent change in volume of the material's crystal structure between the charged and discharged states. The voltage and gravimetric capacity values are plotted in Figure 3 to show the corresponding theoretical
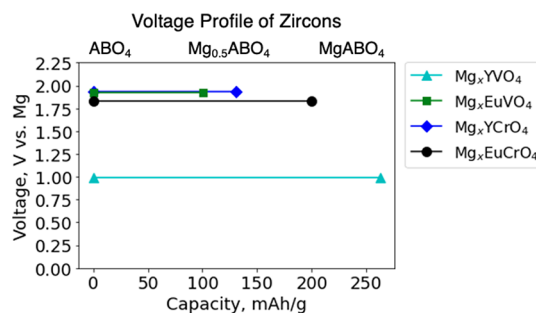

Figure 3. Theoretical voltage profiles based on DFT calculations for zircon YVO₄, EuVO₄, YCrO₄, and EuCrO₄ as Mg intercalation electrodes.

voltage profiles based on DFT calculations for zircon YVO₄, EuVO₄, YCrO₄, and EuCrO₄ as Mg intercalation electrodes. The gravimetric capacities of EuVO₄ and YCrO₄ are significantly lower than those of YVO₄ and EuCrO₄ due to their lower maximum intercalation level of $Mg_{0.5}ABO_4$. Similarly, the predicted volume changes of YVO₄ and EuCrO₄ are greater than EuVO₄ and YCrO₄ due to their higher maximum intercalation level of $MgABO_4$.

DFT-Predicted Mg-Ion Mobility. The Mg sites identified by the insertion algorithm can be used to form a migration graph mapping out a network of connected sites in the host structure.[32] This migration graph analysis enables searching for possible percolating pathways in the intercalation material. In this case, the insertion algorithm and migration graph analysis identified linear pathways consisting of the interstitial sites formed by distorted octahedra and tetrahedra. These sites form one-dimensional channels, which have been previously reported in a crystallography study of the zircon structure.[12] Migration along this percolating pathway is expected to be composed of a series of repeating linear hops between interstitial sites that are approximately 1.5 Å apart. Notably, at the highest Mg concentration, we observed a vacant site between occupied Mg sites along the 1D pathway, implying a Mg–Mg distance of about 3 Å. Images illustrating this pathway in a supercell of zircon YVO₄ are shown in Figure 4.

DFT nudged elastic band (NEB) calculations were performed to evaluate the solid-state Mg-ion mobility along this path in the dilute limit of Mg ions, which in our supercell corresponds to one Mg per 16 formula units. The resulting change in energy as the Mg-ion traverses the linear ~1.5 Å hop in YVO₄, EuVO₄, YCrO₄, and EuCrO₄ is shown in Figure 5. The Mg-ion dilute lattice limit migration barrier is 71 meV for

Table 3. Summary of Theoretical ABO_4 Zircon Electrode Properties Calculated Using DFT Such as Voltage (Compared to the Mg/Mg^{2+} Redox Couple), Gravimetric Capacity (Based on the ABO_4 Molar Mass for the Charged Composition without Mg), and the Change in Volume of the Material's Crystal Structure between the Charged and Discharged State

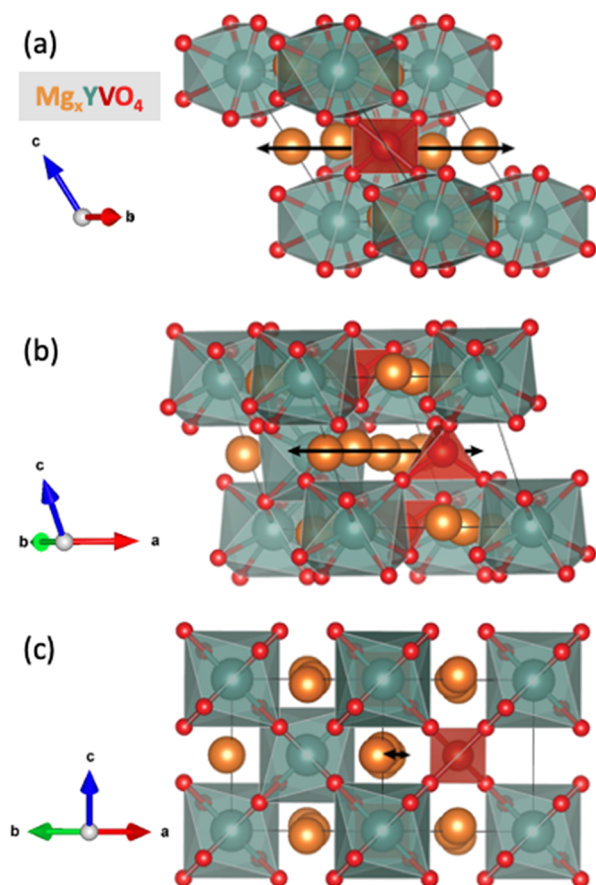| ABO₄ Zircon	Intercalation Reaction	Voltage (V vs Mg/Mg^{2+})	Gravimetric Capacity (mAh/g)	Volume Change (%)
YVO₄ (mp-19133)	$Mg + YVO_4 \Leftrightarrow MgYVO_4$	1.0	263	12
EuVO₄ (mp-22796)	$0.5 Mg + EuVO_4 \Leftrightarrow Mg_{0.5}EuVO_4$	1.9	100	7
YCrO₄ (mp-18825)	$0.5 Mg + YCrO_4 \Leftrightarrow Mg_{0.5}YCrO_4$	1.9	131	6
EuCrO₄ (mp-22586)	$Mg + EuCrO_4 \Leftrightarrow MgEuCrO_4$	1.8	200	10

Figure 4. YVO_4 zircon supercell illustrating the one-dimensional linear diffusion pathway shown from three different perspectives. In (a) the diffusion pathway is in the plane of the page, while in (c), the structure is rotated 90° and the diffusion pathway is perpendicular to the plane of the page. Panel (b) shows an intermediate perspective rotated 45° from (a) and (c).
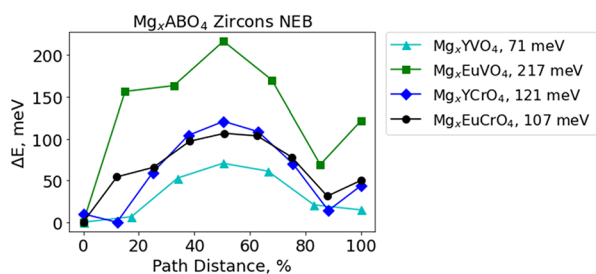

Figure 5. Energy profiles determined by DFT-NEB for Mg^{2+} migration across the characteristic ~1.5 Å linear hop at the dilute lattice limit (single Mg-ion in supercell) for zircon YVO_4, $EuVO_4$, $YCrO_4$, and $EuCrO_4$.

YVO_4, 217 meV for $EuVO_4$, 121 meV for $YCrO_4$, and 107 meV for $EuCrO_4$. These migration barrier values are all remarkably low for Mg^{2+}. As a point of comparison, previous work has reported that migration barriers <650 meV would correspond to intrinsic ionic mobility sufficient for room temperature C/2 cycling with nanosized particles.[8] The dilute Mg-ion migration barrier was calculated using the same methods for Chevrel $Mg_xMo_6S_8$, and the first prototype Mg cathode is 565 meV. Chevrel $Mg_xMo_6S_8$ is the first Mg cathode experimentally demonstrated to have sufficient rate capability for repeated cycling at room temperature.[1,33] To our

knowledge, the lowest calculated Mg^{2+} migration barrier that has ever been reported is ~80 meV, for a theoretical, to date unrealized compound, $Mo_3(PO_4)_3O$.[34] It is encouraging that high Mg-ion mobility is consistently predicted across the broader zircon family and is not limited to a specific chemistry. This suggests that these transport properties are connected to the unique structural characteristics of this family of compounds.

Experimental Synthesis of Zircons. The sol−gel technique has been shown to be successful in the synthesis of YVO_4 nanopowders.[35] In this study, a similar recipe was used to synthesize three different zircon ABO_4 compounds (YVO_4, $EuVO_4$, and $EuCrO_4$) using oxide precursors as the source of the B-site transition metals (V, Cr) and nitrate-based precursors as the source of A-site 3+ cations (Y, Eu). Further synthesis details are included in the "Methods" section. The phase purity of the synthesized samples was evaluated through X-ray diffraction (XRD) studies and subsequent Rietveld refinement analysis, with the results shown in Figure 6. The XRD patterns of zircon YVO_4, $EuVO_4$, and $EuCrO_4$ all indicate high phase purity with no detectable crystalline impurities. The synthesis calcination time was limited to 30 min for 500 °C to obtain smaller particle sizes with a homogeneous distribution compared to classic solid-state synthesis techniques (which require long sintering times of 20−30 h at high temperatures such as 800 °C). A sample scanning electron microscopy (SEM) image of YVO_4 is provided in Figure 6d. SEM images of the zircon YVO_4, $EuVO_4$, and $EuCrO_4$ samples revealed that all samples had a homogeneous particle size distribution with an average particle size range of 50−60 nm.

Electrochemical Cycling of Synthesized Zircons as Mg Cathodes. Coin cells were prepared for the synthesized zircon YVO_4, $EuVO_4$, and $EuCrO_4$ samples. The coin cells used an activated carbon (AC) anode and custom electrolyte, 0.5 M $Mg(TFSI)2$ in 1 M diglyme in 1,1,2,2-tetrafluoroethyl-2,2,3,3-tetrafluoropropyl ether (TTE). The coin cells were tested at 50 °C with a current density of 2 mA/g in the voltage range of −1.5 to 1.1 V vs AC. The resulting electrochemical cycling data for all three samples under the same cycling protocol and conditions are shown in Figure 7. The first cycle measured discharge capacities were 62 mAh/g for YVO_4, 50 mAh/g for $EuVO_4$, and 59 mAh/g for $EuCrO_4$. The 2nd cycle measured discharge capacities were 43 mAh/g for YVO_4, 55 mAh/g for $EuVO_4$, and 42 mAh/g for $EuCrO_4$. The 10th cycle measured discharge capacities were 50 mAh/g for YVO_4, 48 mAh/g for $EuVO_4$, and 30 mAh/g for $EuCrO_4$. YVO_4 and $EuCrO_4$ showed notable capacity losses after the first cycle while $EuVO_4$ showed the best capacity retention

Generally, the vanadium-based zircons showed better reversible cycling compared to $EuCrO_4$, which exhibited the lowest capacity retention of the three samples. XRD performed on $EuCrO_4$ and YVO_4 after electrochemical cycling confirmed that the tetragonal zircon phase was the only crystalline phase present after cycling. These results are included in the Supporting Information. The ex situ XRD verified that the poor performance of $EuCrO_4$ is not related to any significant bulk phase transition upon cycling, though it cannot exclude whether some part of the material dissolves in the electrolyte or makes an amorphous product.

Confirming Mg Intercalation with EDS. Ex situ SEM-EDS analysis was performed to verify Mg intercalation after electrochemical cycling in the synthesized zircon YVO_4, $EuVO_4$, and $EuCrO_4$ samples. New coin cells were prepared
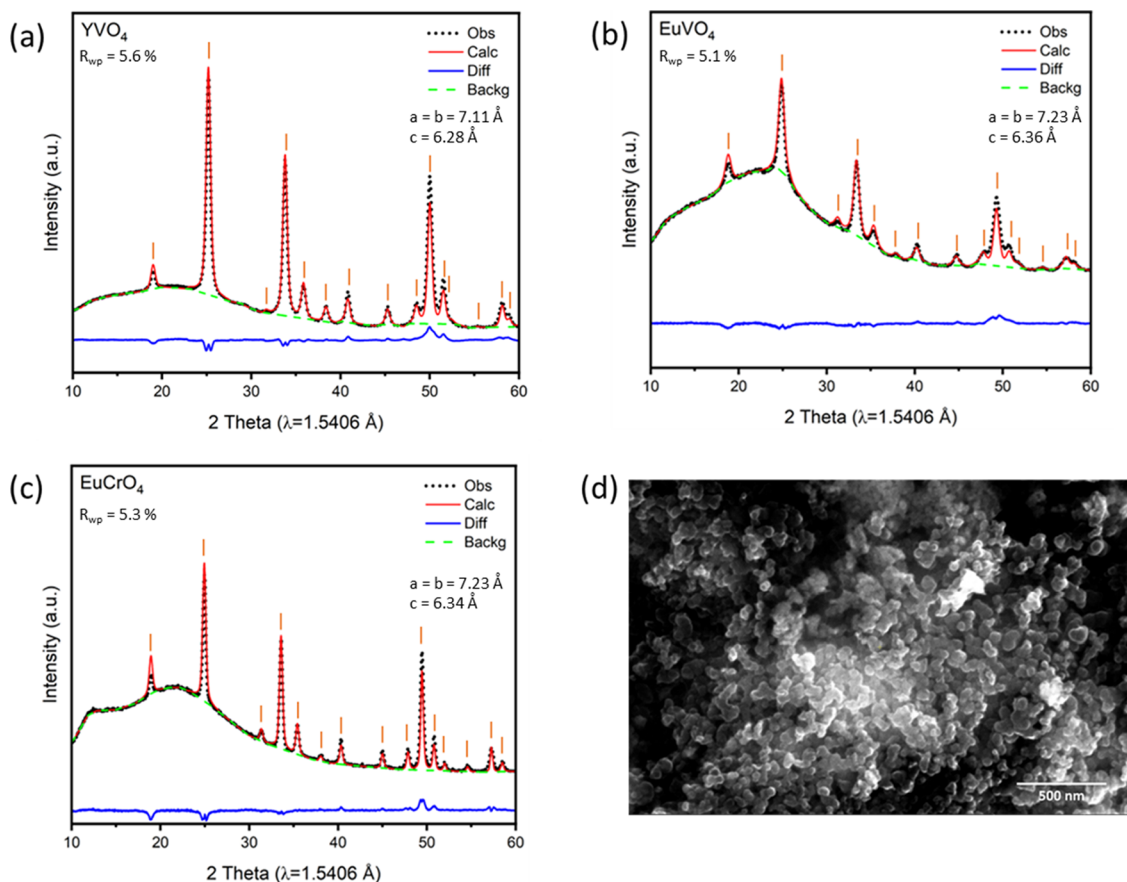
Figure 6. XRD results of the as-synthesized zircon (a) YVO_4, (b) $EuVO_4$, and (c) $EuCrO_4$ compounds. (d) SEM image of synthesized zircon YVO_4 sample after calcination at 500 °C for 30 min.

to harvest the cathode materials for analysis after the 1st charge cycle and after the 1st discharge cycle. These ex situ SEM-EDS results are reported in Table 4. They confirm that after the 1st discharge down to −1.5 V vs AC, Mg is present in all three samples, and the Mg atomic percentages is consistent with the capacities measured from electrochemical testing. The EDS data furthermore shows that after the 1st full cycle (1st discharge then 1st charge) Mg is successfully extracted in all three samples (with atomic percentage < 1% remaining). Overall, the ex situ SEM-EDS measurements confirmed successful Mg intercalation in the zircon YVO_4, $EuVO_4$, and $EuCrO_4$ samples.

DISCUSSION

We propose that the remarkably high Mg-ion mobility predicted based on these reported NEB results is due to the unique structural motif found in ABO_4 zircon materials. As previously introduced, the zircon structure exhibits one-dimensional channels of interstitial sites composed of over-lapping, distorted octahedra and tetrahedrons.[12] This one-dimensional channel in the zircon structure (see Figure 8) enables ionic transport via unusually short, repeating ~1.5 Å hops between interlocking octahedra and tetrahedra. Oxygens form a repeating pattern along the channel and can be divided into pairs of atoms (A, B, C, and D), which rotate as one moves along the migration direction which is depicted in Figure 8b,c. The interstitial distorted octahedral sites can be visualized by considering three adjacent pairs of oxygens (six atoms total), while the tetrahedral sites are formed by two

adjacent pairs of oxygens (four atoms total). Figure 8d shows the two tetrahedral sites (e.g., AB and BC) contained within one distorted octahedra (e.g., ABC) which are shaded. Two neighboring distorted octahedral sites (e.g., ABC and BCD) share four atoms (e.g., B1, B2, C1, and C2) and overlap in volume through the shared tetrahedral site (BC).

Furthermore, the distortion of the octahedral interstitial site in the zircon structure reduces the preference of the Mg-ion for this site. Minimizing the change in coordination of the migrating ion along the diffusion pathway correlates with smaller site energy differences, resulting in favorable, lower migration barriers because of the resulting flatter energetic landscape.[8,34] Large changes along the path to lower coordination numbers, such as 2 and 3, have been shown to correspond to the most unfavorable sites along a diffusion pathway for multivalent ions in a variety of materials.[2,8,34] This makes overlapping distorted octahedral and tetrahedral interstitial sites of zircon particularly well suited for Mg-ion transport. The interlocked interstitial sites of the one-dimensional zircon diffusion channels result in a "6-5-4" change in coordination, which corresponds to significantly less coordination change as compared to the typical "6-3-4" change in coordination found in diffusion pathways composed of face-sharing tetrahedral and octahedral sites (see Figure 1). The intermediate coordination of 5 in the zircon structure is much more favorable than 3 because migrating ions avoid squeezing through a plane of anions, which usually corresponds to higher energies.[2]
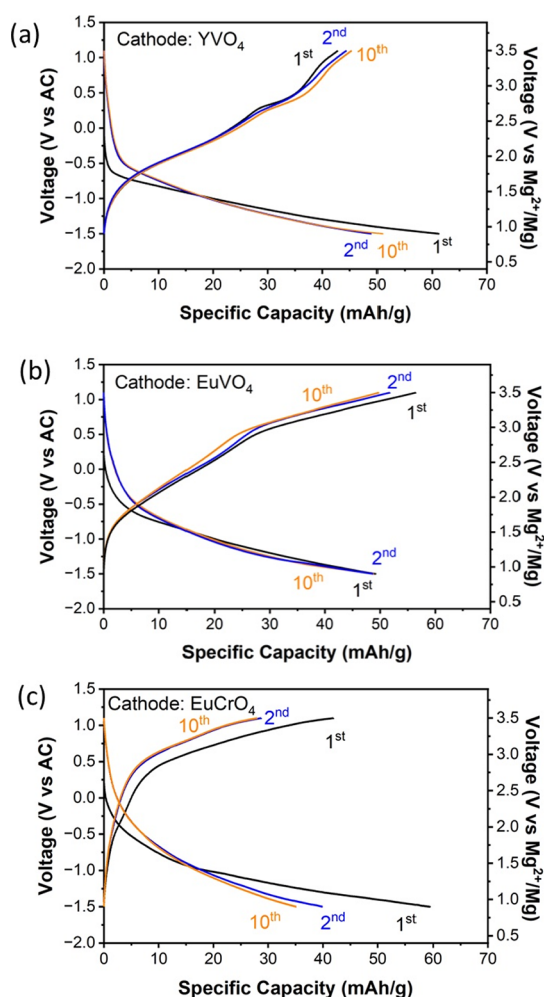
Figure 7. Experimentally measured charge and discharge voltage profiles of zircon (a) YVO_4, (b) $EuVO_4$, and (c) $EuCrO_4$ as Mg cathodes against activated carbon anodes at 50 °C with a current density of 2 mA/g.

Figure 8. Depiction of the unique zircon structural motif, which has one-dimensional linear channels of interstitial sites composed of distorted octahedra and tetrahedrons that are overlapping in volume. The YVO_4 zircon supercell crystal structure with the migration direction perpendicular to the plane of the page is shown in panel (a). The same perspective is used in (b) to depict the repeating pattern of oxygens along the channel, which can be divided into pairs of atoms (A, B, C, and D), which rotate along the migration direction. This repeating pattern of oxygen atoms where the migration direction is within the plane of the page is shown in (c) with the addition of solid colored (orange, blue, and black) lines to represent distances of the same length and dashed gray lines marking the pairs of oxygen atoms (A, B, C, and D). The distorted octahedra sites along the diffusion pathway are shown in (d) with shading to show the overlapping volumes from four shared atoms (forming a tetrahedra) between distorted octahedra.

While the Mg-ion transport properties of the zircon family are attractive, this structure presents other disadvantages when considered as an intercalation cathode. The zircon structure exhibits one-dimensional diffusion channels which usually requires nanosized primary particles in practical applications, due to the inevitable blocking of the transport passages by intrinsic anti-site defects in larger particles.[36] Indeed, our first attempts to synthesize the zircon materials by solid-state methods resulted in micron-sized particles, which exhibited very poor electrochemical performance. Furthermore, the theoretically predicted and experimentally measured voltages are also too low to be attractive as high-performance Mg ca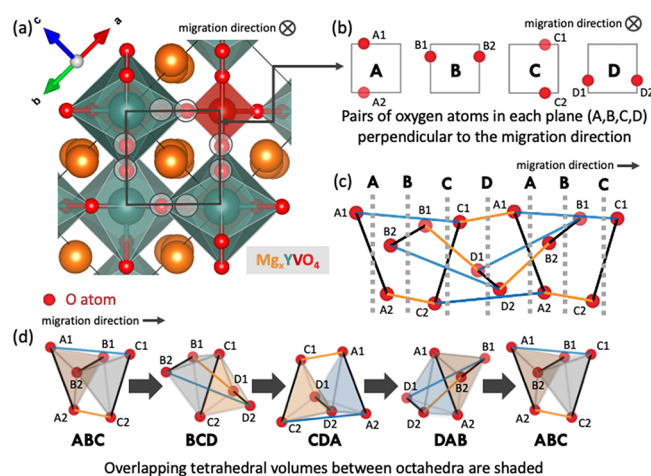thodes. Finally, in addition to these limitations, DFT calculations predicted poor phase stability for zircon materials upon Mg-ion intercalation, except for $EuVO_4$.

We suggest that the poor phase stability of zircon materials when discharge is connected to the reduction of the tetrahedral transition metal (B atom) in the ABO_4 zircon structure. Small, higher valence transition metals (e.g., V^{5+}, Cr^{6+}, and Cr^{5+}) favor tetrahedral coordination while lower valence transition metals (e.g., V^{4+}, V^{3+}, Cr^{4+}, and Cr^{3+}) favor octahedral coordination.[7] Therefore, when the redox active transition metal is reduced to a lower oxidation state upon Mg-ion intercalation ($V^{5+} \rightarrow V^{4+}$ or $Cr^{5+} \rightarrow Cr^{4+}$), the tetrahedral coordination becomes less stable and cation migration into the diffusion channel is likely.

While zircon $EuVO_4$ demonstrated the most stable electrochemical performance and capacity retention, its experimentally measured capacity (~50 mAh/g) is still lower than expected (100 mAh/g). Zircon YVO_4 exhibited the highest first cycle discharge capacity (62 mAh/g) of the three synthesized zircons, however, the measured capacity is lower than expected. The higher initial capacity measured for YVO_4

Table 4. Elemental Compositions of the Ex Situ ABO_4 Zircon Samples Collected after the 1st Discharged Cycle and the 1st Full Cycle (1st Discharge Then 1st Charge) Measured by SEM-EDS Analysis

	YVO₄		EuVO₄		EuCrO₄	
	After 1st Discharge	After 1st Charge	After 1st Discharge	After 1st Charge	After 1st Discharge	After 1st Charge
ABO₄ Zircon			Atomic Percentages (%)			
Mg	8.94	0.92	7.52	0.54	6.24	0.86
A site (Y, Eu)	44.86	48.22	45.58	49.70	47.20	50.23
B site (V, Cr)	46.20	50.86	46.90	49.76	46.56	48.91

correlates with its highest theoretical capacity (263 mAh/g for Mg + YVO$_4$ ⇔ MgYVO$_4$) which is attributed to the significantly smaller atomic weight of Y compared to Eu and the higher maximum intercalation level predicted. This initial work focuses on evaluating the viability of zircon materials as Mg cathodes, but further investigations into the causes behind the limited electrochemical performance of these materials are clearly needed.

CONCLUSIONS

In conclusion, this work evaluated the viability of 4 zircons (YVO$_4$, EuVO$_4$, YCrO$_4$, EuCrO$_4$) as Mg intercalation cathodes with DFT. Among these materials, three (YVO$_4$, EuVO$_4$, and EuCrO$_4$) were successfully synthesized and experimentally tested to validate their electrochemical properties. While all four zircon compounds were calculated to exhibit remarkably good Mg-ion transport with low Mg^{2+} migration barriers (<250 meV), zircon EuVO$_4$ has the best predicted phase stability and electrochemical performance upon experimental testing. The promising Mg-ion transport properties of the zircon family are attribute to their unique "6-5-4" change in coordination of the migrating ion along the diffusion pathway, which is created by overlapping interstitial distorted octahedral and tetrahedral sites. As such, the zircon structure presents exciting design motifs for promoting Mg-ion mobility; however, the one-dimensional diffusion pathways, limited voltages, and tetrahedral coordination of the redox-active transition metal likely limit their viability as suitable Mg cathodes. While zircons may not serve as promising high-performance Mg cathodes, the structure family offers useful insights into material design rules based on polyhedra with overlapping volumes for improving multivalent ion transport.

METHODS

DFT Calculations for Phase Stability and Electrode Properties. Unit cell structures of zircon YVO$_4$ (mp-19133), EuVO$_4$ (mp-22796), YCrO$_4$ (mp-18825), and EuCrO$_4$ (mp-22586) were sourced from the Materials Project database.[14] Single Mg atoms were inserted into each unit cell structure (corresponding to a composition of Mg$_{0.5}$ABO$_4$) before performing a DFT relaxation based on the insertion algorithm[25] which has been implemented as a workflow in the Python package, atomate.[37] If the host framework remained intact according to the structure matching capabilities in pymatgen,[26] a second Mg atom was inserted into the unit cell structure. A maximum of two Mg atoms (corresponding to a composition of MgABO$_4$) insertions were attempted to avoid exceeding the redox capabilities of the material where the B transition metal cannot be further reduced than B^{5+} → B^{3+}. Theoretical voltages were calculated using $\Delta G_{rxn} = -nFV$, which represents the energy difference of the intercalation reaction. ΔG_{rxn} is determined using the energies from DFT. F is Faraday's constant and $n = 2$ for a Mg-ion intercalation reaction.

DFT relaxations were performed using the Vienna Ab initio Software Package (VASP) with the exchange correlation approximated with the Perdew−Burke−Ernzerhof (PBE) generalized gradient approximation (GGA). Hubbard U corrections of $U_V = 3.25$ and $U_{Cr} = 3.7$ eV were applied to match the Materials Project data and "MPRelaxSet" in pymatgen.[26] "MPRelaxSet" in pymatgen[26] was used to set the pseudopotentials used for the DFT relaxations. The total energy was sampled using a Monkhorst−Pack mesh with k-point density of 64 Å^{-3}. Projector augmented-wave theory combined with a well-converged plane-wave cutoff of 520 eV was used to describe the wave functions. The convergence threshold of the total energy was set to 0.00005 eV/atom and a force tolerance of 0.05 eV/Å.

NEB + DFT Calculations. NEB + DFT was used for calculating the migration barriers of zircon YVO$_4$, EuVO$_4$, YCrO$_4$, and EuCrO$_4$. These calculations were performed using VASP with the addition of Transition State Tools for VASP software.[38] 2 × 2 × 2 supercells were created from the unit cell structures and then transformed to orient the linear diffusion pathway and one-dimensional channels in the zircon structure along the b-axis. The migration barrier was evaluated at the dilute lattice limit where there is a single Mg atom in the host framework, which resulted in supercell structures with a total of 97 atoms. The supercell lattice parameters were all >10 Å to eliminate the possibility of any fictios self-interaction effects on the migration ion due to periodic boundary conditions.

"MPRelaxSet" in pymatgen[26] was used to set the DFT calculation parameters with the following exceptions. No Hubbard U corrections were applied as there is no conclusive evidence that GGA+U performs better than GGA when investigating ion migration with NEB.[39−42] Gaussian smearing was used. No symmetry but $\Psi_k = \Psi^*_{-k}$ was assumed to reduce sampling of the Brillouin zone. An additional support grid for the evaluation of the augmentation charge was applied. A minimum of four electronic self-consistency steps were required. Endpoint structure relaxations were converged with a total energy of 0.00005 eV and a force tolerance of 0.01 eV/Å cut-off criteria. A linear interpolation of images was used between the relaxed endpoints. During the NEB calculation, images were converged to a total energy of 0.00005 eV and a force tolerance of 0.05 eV/Å cut-off criteria.

Sol−Gel Synthesis. The synthesis method was derived from previous work on YVO$_4$ nanopowders.[35] Zircon EuCrO$_4$, YVO$_4$, and EuVO$_4$ compounds were synthesized via sol−gel technique using stoichiometric ratios of Eu:Cr, Y:V, and Eu:V precursors, respectively. Europium nitrate pentahydrate (Eu(NO$_3$)$_3$·5H$_2$O), yttrium nitrate hexahydrate (Y(NO$_3$)$_3$·6H$_2$O), vanadium pentoxide (V$_2$O$_5$), and chromium(VI) oxide (CrO$_3$) powders were purchased from Sigma-Aldrich and used without further purification. For gelation, the powders of the transition metal source depending on the targeted compound were slowly dissolved in hydrogen peroxide (H$_2$O$_2$ from Sigma-Aldrich). For the synthesis of EuVO$_4$ and YVO$_4$, 0.3 g of V$_2$O$_5$ was placed in a glass beaker, and 25 mL H$_2$O$_2$ was added dropwise. The addition of H$_2$O$_2$ was done very slowly to prevent excessive bubbling and loss of the material. After 10 min, a red solution was formed, and then nitrate-based Y(NO$_3$)$_3$·6H$_2$O (for the synthesis of YVO$_4$) or Eu(NO$_3$)$_3$·5H$_2$O (for the synthesis of EuVO$_4$) was added. The amount of nitrate precursor was calculated according to the targeted 1:1 ratio of Y:V or Eu:V, respectively. For this purpose, 1.263 g of Y(NO$_3$)$_3$·6H$_2$O and 5 g of citric acid were added to the red solution. The resultant mixture was placed in a hot-plate and continuously stirred at 60 °C until it formed a viscous blue-colored gel. As a final step, the gel was collected and placed in an alumina crucible and calcined at 500 °C for 30 min. The same process was applied to synthesize zircon EuCrO$_4$ by changing the precursors accordingly.

XRD and SEM-EDS Characterization. The phase identification of the synthesized zircon EuCrO$_4$, YVO$_4$, and EuVO$_4$ samples, and the structural changes upon cycling as Mg cathodes were observed by ex-situ XRD using a Rigaku MiniFlex 600 diffractometer with Cu K$_\alpha$ radiation (λ = 1.54178 Å) in the 2θ range of 10°−60°. Rietveld refinement made using the PANalytical X'pert HighScore Plus software. EDS analysis and SEM images were collected using a Zeiss Gemini Ultra-55 analytical field-emission SEM at the Molecular Foundry at Lawrence Berkeley National Lab.

Electrochemical Cycling. Cathode films were prepared by mixing a 7:2:1 ratio of the zircon active material, carbon black (Timcal, SUPER C65), and polytetrafluoroethylene (PTFE from DuPont, Teflon 8A). Anode films were prepared by mixing a weight ratio of 8:1:1 of activated carbon (Sigma), carbon black (Timcal, SUPER C65), and PTFE (DuPont, Teflon 8A). The mixtures were rolled to form thin film electrodes with surface areas of 1 cm^2. Coin cells were prepared with a loading density of 3 mg/cm^2 for the cathode and 20 mg/cm^2 for the anode. All work was performed in an argon-filled glovebox.

The electrolyte was prepared by drying magnesium(II) bis-(trifluoromethanesulfonyl)imide (Mg(TFSI)$_2$ from Solvionic with

99.5% purity) salt at 170 °C overnight in an argon-filled glovebox. The dried salt was then used to form a 0.5 M Mg(TFSI)$_2$, 1 M diglyme (99.5%, Sigma-Aldrich) solution in 1,1,2,2-tetrafluoroethyl-2,2,3,3-tetrafluoropropyl ether (TTE from TCI Chemicals). The electrolyte and its components were always kept in an argon-filled glovebox.

Electrochemical testing was performed in coin cells made from the cathode and anode thin films using a Whatman glass microfiber filter along with the prepared 0.5 M Mg(TFSI)$_2$ and 1 M diglyme in TTE electrolyte. Galvanostatic cycling was performed at 50 °C using an Arbin battery tester. The coin cells were cycled with a current density of 2 mA/g. Ex situ samples were collected after disassembling the coin cells and washing the cathode thin films with diglyme in an argon-filled glovebox.

■ ASSOCIATED CONTENT

Ⓢ Supporting Information

The Supporting Information is available free of charge at https://pubs.acs.org/doi/10.1021/acsami.3c05964.

> SEM-EDS data on zircon EuCrO$_4$ sample after electrochemical cycling; ex situ XRD data on zircon EuCrO$_4$ sample after electrochemical cycling; and ex situ XRD data on zircon YVO$_4$ sample after electrochemical cycling (PDF)

■ AUTHOR INFORMATION

Corresponding Author

Kristin A. Persson − *Department of Materials Science and Engineering, University of California, Berkeley 94720, United States; Materials Sciences Division, Lawrence Berkeley National Laboratory, Berkeley 94720, United States;* ⓘ orcid.org/0000-0003-2495-5509; Email: kapersson@lbl.gov

Authors

Ann Rutt − *Department of Materials Science and Engineering, University of California, Berkeley 94720, United States;* ⓘ orcid.org/0000-0001-6534-454X

Dogancan Sari − *Department of Materials Science and Engineering, University of California, Berkeley 94720, United States*

Qian Chen − *Materials Sciences Division, Lawrence Berkeley National Laboratory, Berkeley 94720, United States;* ⓘ orcid.org/0009-0009-3557-0744

Jiyoon Kim − *Department of Materials Science and Engineering, University of California, Berkeley 94720, United States;* ⓘ orcid.org/0000-0002-0383-1198

Gerbrand Ceder − *Department of Materials Science and Engineering, University of California, Berkeley 94720, United States; Materials Sciences Division, Lawrence Berkeley National Laboratory, Berkeley 94720, United States;* ⓘ orcid.org/0000-0001-9275-3605

Complete contact information is available at:
https://pubs.acs.org/10.1021/acsami.3c05964

Author Contributions

§A.R. and D.S. contributed equally to this study.

Author Contributions

A.R. led the computational work presented and was the primary author of this manuscript. D.S. led and contributed writing describing the experimental work presented. Q.C. and J.K. both assisted with the computation work and manuscript editing. G.C. supervised the experimental work, provided input on computational work, and contributed to manuscript preparation. K.A.P. supervised the computational work and contributed to manuscript preparation.

Notes

The authors declare no competing financial interest.

■ ACKNOWLEDGMENTS

■ REFERENCES

(1) Aurbach, D.; Lu, Z.; Schechter, A.; Gofer, Y.; Gizbar, H.; Turgeman, R.; Cohen, Y.; Moshkovich, M.; Levi, E. Prototype Systems for Rechargeable Magnesium Batteries. *Nature* **2000**, *407*, 724−727.

(2) Rutt, A.; Shen, J.-X.; Horton, M.; Kim, J.; Lin, J.; Persson, K. A. Expanding the Material Search Space for Multivalent Cathodes. *ACS Appl. Mater. Interfaces* **2022**, *14*, 44367−44376.

(3) Yang, R.; Yao, W.; Tang, B.; Zhang, F.; Lei, X.; Lee, C.-S.; Tang, Y. Development and Challenges of Electrode Materials for Rechargeable Mg Batteries. *Energy Storage Mater.* **2021**, *42*, 687−704.

(4) Canepa, P.; Sai Gautam, G.; Hannah, D. C.; Malik, R.; Liu, M.; Gallagher, K. G.; Persson, K. A.; Ceder, G. Odyssey of Multivalent Cathode Materials: Open Questions and Future Challenges. *Chem. Rev.* **2017**, *117*, 4287−4341.

(5) Tian, Y.; Zeng, G.; Rutt, A.; Shi, T.; Kim, H.; Wang, J.; Koettgen, J.; Sun, Y.; Ouyang, B.; Chen, T.; Lun, Z.; Rong, Z.; Persson, K.; Ceder, G. Promises and Challenges of Next-Generation "Beyond Li-Ion" Batteries for Electric Vehicles and Grid Decarbonization. *Chem. Rev.* **2021**, *121*, 1623−1669.

(6) Brown, I. D. What Factors Determine Cation Coordination Numbers? *Acta Crystallogr. B* **1988**, *44*, 545−553.

(7) Waroquiers, D.; Gonze, X.; Rignanese, G.-M.; Welker-Nieuwoudt, C.; Rosowski, F.; Göbel, M.; Schenk, S.; Degelmann, P.; André, R.; Glaum, R.; Hautier, G. Statistical Analysis of Coordination Environments in Oxides. *Chem. Mater.* **2017**, *29*, 8346−8360.

(8) Rong, Z.; Malik, R.; Canepa, P.; Sai Gautam, G.; Liu, M.; Jain, A.; Persson, K.; Ceder, G. Materials Design Rules for Multivalent Ion Mobility in Intercalation Structures. *Chem. Mater.* **2015**, *27*, 6016−6021.

(9) Koettgen, J.; Bartel, C. J.; Ceder, G. Computational Investigation of Chalcogenide Spinel Conductors for All-Solid-State Mg Batteries. *Chem. Commun.* **2020**, *56*, 1952−1955.

(10) Canepa, P.; Bo, S.-H.; Sai Gautam, G.; Key, B.; Richards, W. D.; Shi, T.; Tian, Y.; Wang, Y.; Li, J.; Ceder, G. High Magnesium Mobility in Ternary Spinel Chalcogenides. *Nat. Commun.* **2017**, *8*, 1759.

(11) Liu, M.; Jain, A.; Rong, Z.; Qu, X.; Canepa, P.; Malik, R.; Ceder, G.; Persson, K. A. Evaluation of Sulfur Spinel Compounds for Multivalent Battery Cathode Applications. *Energy Environ. Sci.* **2016**, *9*, 3201−3209.

(12) Finch, R. J.; Hanchar, J. M. Structure and Chemistry of Zircon and Zircon-Group Minerals. *Rev. Mineral. Geochem.* **2003**, *53*, 1−25.

(13) Long, Y. W.; Yang, L. X.; Yu, Y.; Li, F. Y.; Yu, R. C.; Jin, C. Q. Synthesis, Structure, Magnetism and Specific Heat of YCrO4 and Its Zircon-to-Scheelite Phase Transition. *Phys. Rev. B: Condens. Matter Mater. Phys.* **2007**, *75*, No. 104402.

(14) Gunter, D.; Cholia, S.; Jain, A.; Kocher, M.; Persson, K.; Ramakrishnan, L.; Ong, S. P.; Ceder, G. Community Accessible Datastore of High-Throughput Calculations: Experiences from the Materials Project. In *2012 SC Companion: High Performance Computing, Networking Storage and Analysis*; IEEE, 2012; pp 1244−1251, DOI: 10.1109/SC.Companion.2012.150.

(15) Huang, Z.; Zhang, L.; Pan, W. Synthesis, Structure, Elastic Properties, Lattice Dynamics and Thermodynamics of YVO4 Polymorphs from Experiments and Density Functional Theory Calculation. *J. Alloys Compd.* **2013**, *580*, 544−549.

(16) Huang, Z.; Feng, J.; Pan, W. Theoretical Investigations of the Physical Properties of Zircon-Type YVO4. *J. Solid State Chem.* **2012**, *185*, 42−48.

(17) Errandonea, D.; Lacomba-Perales, R.; Ruiz-Fuertes, J.; Segura, A.; Achary, S. N.; Tyagi, A. K. High-Pressure Structural Investigation of Several Zircon-Type Orthovanadates. *Phys. Rev. B: Condens. Matter Mater. Phys.* **2009**, *79*, No. 184104.

(18) Li, L.-P.; Li, G.-S.; Xue, Y.-F.; Inomata, H. Structure, Luminescence, and Transport Properties of EuVO4. *J. Electrochem. Soc.* **2001**, *148*, J45.

(19) Ranaut, D.; Mukherjee, K. Van Vleck Paramagnetism and Enhancement of Effective Moment with Magnetic Field in Rare Earth Orthovanadate EuVO4. *Phys. Lett. A* **2023**, *465*, No. 128710.

(20) Errandonea, D.; Kumar, R.; López-Solano, J.; Rodríguez-Hernández, P.; Muñoz, A.; Rabie, M. G.; Sáez Puche, R. Experimental and Theoretical Study of Structural Properties and Phase Transitions in YAsO4 and YCrO4. *Phys. Rev. B: Condens. Matter Mater. Phys.* **2011**, *83*, No. 134109.

(21) Konno, H.; Aoki, Y.; Klencsár, Z.; Vértes, A.; Wakeshima, M.; Tezuka, K.; Hinatsu, Y. Structure of EuCrO4 and Its Electronic and Magnetic Properties. *Bull. Chem. Soc. Jpn.* **2001**, *74*, 2335−2341.

(22) Morales-Sánchez, A.; Fernández, F.; Sáez-Puche, R. Magnetic Properties of Rare Earth Chromates RCrO4 (R=Nd, Sm and Eu). *J. Alloys Compd.* **1993**, *201*, 161−165.

(23) Esaka, T.; Kobayashi, Y.; Obata, H.; Iwahara, H. Cation Conduction in Zircon-Type Solid Solution Based on YPO4. *Solid State Ionics* **1989**, *34*, 287−291.

(24) Amezawa, K.; Tomii, Y.; Yamamoto, N. High Temperature Protonic Conduction in Ca-Doped YPO4. *Solid State Ionics* **2003**, *162−163*, 175−180.

(25) Shen, J.; Horton, M.; Persson, K. A. A Charge-Density-Based General Cation Insertion Algorithm for Generating New Li-Ion Cathode Materials. *NPJ Comput. Mater.* **2020**, *6*, 161.

(26) Ong, S. P.; Richards, W. D.; Jain, A.; Hautier, G.; Kocher, M.; Cholia, S.; Gunter, D.; Chevrier, V. L.; Persson, K. A.; Ceder, G. Python Materials Genomics (Pymatgen): A Robust, Open-Source Python Library for Materials Analysis. *Comput. Mater. Sci.* **2013**, *68*, 314−319.

(27) Ong, S. P.; Wang, L.; Kang, B.; Ceder, G. Li−Fe−P−O2 Phase Diagram from First Principles Calculations. *Chem. Mater.* **2008**, *20*, 1798−1807.

(28) Hautier, G.; Ong, S. P.; Jain, A.; Moore, C. J.; Ceder, G. Accuracy of Density Functional Theory in Predicting Formation Energies of Ternary Oxides from Binary Oxides and Its Implication on Phase Stability. *Phys. Rev. B* **2012**, *85*, No. 155208.

(29) Wang, A.; Kingsbury, R.; McDermott, M.; Horton, M.; Jain, A.; Ong, S. P.; Dwaraknath, S.; Persson, K. A. A Framework for Quantifying Uncertainty in DFT Energy Corrections. *Sci. Rep.* **2021**, *11*, 15496.

(30) Sun, W.; Dacek, S. T.; Ong, S. P.; Hautier, G.; Jain, A.; Richards, W. D.; Gamst, A. C.; Persson, K. A.; Ceder, G. The Thermodynamic Scale of Inorganic Crystalline Metastability. *Sci. Adv.* **2016**, *2*, No. e1600225.

(31) Aykol, M.; Dwaraknath, S. S.; Sun, W.; Persson, K. A. Thermodynamic Limit for Synthesis of Metastable Inorganic Materials. *Sci. Adv.* **2018**, *4*, No. eaaq0148.

(32) Shen, J.-X.; Li, H. H.; Rutt, A. C.; Horton, M. K.; Persson, K. A. Rapid Discovery of Cathodes, Ionic Conductors and Solid-State Electrolytes through Topological Migration Analysis. 2022, DOI: 10.48550/arXiv.2202.0022.

(33) Aurbach, D.; Suresh, G. S.; Levi, E.; Mitelman, A.; Mizrahi, O.; Chusid, O.; Brunelli, M. Progress in Rechargeable Magnesium Battery Technology. *Adv. Mater.* **2007**, *19*, 4260−4267.

(34) Rong, Z.; Xiao, P.; Liu, M.; Huang, W.; Hannah, D. C.; Scullin, W.; Persson, K. A.; Ceder, G. Fast Mg2+ Diffusion in Mo3(PO4)3O for Mg Batteries. *Chem. Commun.* **2017**, *53*, 7998−8001.

(35) Gangadharachar, R.; Chandrappa, G. T. *Solution Combustion Synthesis of YVO4 Nanopowder Using V2O5.NH2O Gel: Photodegradation Studies. Trans. Indian Ceram. Soc.* **2021**, *80* (1), 47−54, DOI: 10.1080/0371750X.2020.1864664.

(36) Malik, R.; Burch, D.; Bazant, M.; Ceder, G. Particle Size Dependence of the Ionic Diffusivity. *Nano Lett.* **2010**, *10*, 4123−4127.

(37) Mathew, K.; Montoya, J. H.; Faghaninia, A.; Dwarakanath, S.; Aykol, M.; Tang, H.; Chu, I.; Smidt, T.; Bocklund, B.; Horton, M.; Dagdelen, J.; Wood, B.; Liu, Z.-K.; Neaton, J.; Ong, S. P.; Persson, K.; Jain, A. Atomate: A High-Level Interface to Generate, Execute, and Analyze Computational Materials Science Workflows. *Comput. Mater. Sci.* **2017**, *139*, 140−152.

(38) Henkelman, G.; Jónsson, H. Improved Tangent Estimate in the Nudged Elastic Band Method for Finding Minimum Energy Paths and Saddle Points. *J. Chem. Phys.* **2000**, *113*, 9978−9985.

(39) Liu, M.; Rong, Z.; Malik, R.; Canepa, P.; Jain, A.; Ceder, G.; Persson, K. A. Spinel Compounds as Multivalent Battery Cathodes: A Systematic Evaluation Based on Ab Initio Calculations. *Energy Environ. Sci.* **2015**, *8*, 964−974.

(40) Dathar, G. K. P.; Sheppard, D.; Stevenson, K. J.; Henkelman, G. Calculations of Li-Ion Diffusion in Olivine Phosphates. *Chem. Mater.* **2011**, *23*, 4032−4037.

(41) Ong, S. P.; Chevrier, V. L.; Hautier, G.; Jain, A.; Moore, C.; Kim, S.; Ma, X.; Ceder, G. Voltage, Stability and Diffusion Barrier Differences between Sodium-Ion and Lithium-Ion Intercalation Materials. *Energy Environ. Sci.* **2011**, *4*, 3680.

(42) Morgan, D.; Van der Ven, A.; Ceder, G. Li Conductivity in LixMPO4 (M = Mn, Fe, Co, Ni) Olivine Materials. *Electrochem. Solid-State Lett.* **2004**, *7*, A30.